Ultrasonics Sonochemistry 73 (2021) 105541

Contents lists available at ScienceDirect

Ultrasonics Sonochemistry

journal homepage: www.elsevier.com/locate/ultson

Copper molybdate synthesized by sonochemistry route at room temperature as an efficient solid catalyst for esterification of oleic acid

J.L. Silva Junior [a,1], F.X. Nobre [a,b,1,*], F.A. de Freitas [a,c], T.A.F. de Carvalho [d], S.S. de Barros [e], M. C. Nascimento [a], L. Manzato [f], J.M.E. Matos [d], W.R. Brito [a], Y. Leyet [e,g], P.R.C. Couceiro [a]

[a] Department of Chemistry, Federal University of Amazonas, Manaus 69077-000, Brazil
[b] Federal Institute of Amazonas, Campus Coari, Coari 69460-000, Brazil
[c] Amazon Biotechnology Center – CBA, Industrial District, Manaus 69075-351, Brazil
[d] Department of Chemistry, Federal University of Piauí, Teresina 64049-550, Brazil
[e] Department of Materials Engineering, Federal University of Amazon, 69077-000 Manaus, Brazil
[f] Federal Institute of Amazonas – IFAM, Distrito Industrial, 69.075-351, Manaus, AM, Brazil
[g] LPMaT, Programa de Pós-graduação em Ciência e Engenharia de Materiais, Departamento de Engenharia de Materiais, Universidade Federal do Amazonas, Manaus, Amazonas 69077-000, Brazil

ARTICLE INFO

Keywords:
Lindgrenite
Esterification
Biofuel
Catalysis

ABSTRACT

Copper molybdate nanoplates were synthesized by a sonochemical process at room temperature, which we report as a simple and cost-effective route. Structural analysis of the material by the Rietveld method of X-ray diffraction (XRD) data revealed lindgrenite $Cu_3(MoO_4)_2(OH)_2$ in a single-phase structure. All the vibrational modes characteristic of the space group were identified by Raman vibrational and near-infrared (NIR) spectroscopies. The profile obtained for N_2 adsorption/desorption was type III hysteresis, characteristic of mesoporous materials, with a surface area of 70.77(1) $m^2\ g^{-1}$. The micrographs of the material obtained by scanning electron microscopy showed nanoplates with nanometric sizes and an anisotropic growth aspect. The catalytic activity of lindgrenite was evaluated by esterifying oleic acid with methanol, showing high conversion rate to methyl oleate and good catalyst stability after seven recycling cycles. Above all, the best catalytic performance was reached when we optimized parameters such as oleic acid:methanol molar ratio of 1:5, 5% of catalyst dosage, and reaction time of 5 h, resulting in 98.38% of conversion at 413 K. Therefore, sonochemically synthesized lindgrenite proved to be a high potential material for biofuel production by oleic acid esterification.

1. Introduction

In recent years, government policies related to the use of fossil fuels and their derivatives have intensified due to the ecological impacts caused by the residues resulting from their extraction, processing, and consumption [1]. In this context, investments in several other energy matrices of a renewable nature and products with biodegradable characteristics have driven research aimed at technologies that meet these objectives [2]. Therefore, hydrogen cells [3], biofuels [4], and solar cells [5] are considered promising in energy generation with minor ecological impacts compared to fossil fuels.

Biofuels, which are fuels derived from animal or vegetable matrices, have similarities in energy content compared to fuels derived from petroleum [6]. In general, biofuels are obtained via transesterification reactions from animal fats or vegetable oils and fatty acid esterification [7]. Thus, biofuels combustion provides high energy efficiency with less emission of greenhouse gases [8]. However, due to the esterification or transesterification reactions' energy barrier, catalysts have been a viable alternative to increase the reaction speed and the conversion percentage of the final product [9].

As for the types of catalysts, the so-called solid acid catalysts have specific characteristics of a broad interest in reactions to obtain biofuels [10]. The advantages of solid catalysts over homogeneous catalysts are mainly due to the easy removal of these from the reaction medium, high thermodynamic stability, low or no corrosive effect and the possibility of reuse in several cycles [11].

* Corresponding author at: Federal Institute of Amazonas, Campus Coari, Coari 69460-000, Brazil.
E-mail address: xavier.nobre.ufpi@gmail.com (F.X. Nobre).
[1] These authors have contributed equally to this work.

https://doi.org/10.1016/j.ultsonch.2021.105541
Received 24 June 2020; Received in revised form 21 March 2021; Accepted 23 March 2021
Available online 26 March 2021

Solid acid catalysts composed of transition metals have in their structure groups of atoms called Bronsted bases or Lewis acids [12]. According to Tao *et al.*[13], the acid and base sites present on the catalyst surface directly affect the synthesis of biodiesel. In the case of Brønsted acids, these have greater activity in the esterification reactions, while Lewis acids are more efficient in transesterification [14]. These referred groups interact efficiently with polar groups of the substrate molecules (oils, fats and fatty acids), conducting the esterification and transesterification reactions under a lower energy barrier [15]. Besides, the surface area, pore diameter and volume, surface energy, and particle size of solid catalysts positively influence these materials' catalytic properties [16].

According to Changmai et al. [17], the use of heterogeneous acid catalysts may be considered a viable alternative to reduce the costs of biodiesel production. Heterogeneous acid catalysts have advantages related to their easy separation of products [18]. Besides the possibility of recovery and reuse of the catalyst, they minimize problems related to corrosion and toxicity [11]. This class of catalysts includes, among others, inorganic oxides [19], enzymes [20], ion exchange resins [21] and zeolites [22]. However, a high catalytic performance has been exhibited by copper oxide [23] and molybdenum oxide [24] in the transesterification of vegetable oils. Also, they are easily synthesized by conventional and low-cost methods, which reinforces the interest in these compounds [25,26]. In this context, although there is a significant catalytic properties of the polymorphs of copper molybdate, specifically in the esterification or transesterification of biomolecules to obtain biodiesel, they are absent in the literature so far [27].

Copper molybdate ($CuMoO_4$) is a semiconductor widely known and reported in the literature due to its thermochromic and piezochromic properties [27-31]. As stated by Rahimi-Nasrabadi *et al.* [28], molybdate anions (MoO_4^{2-}) form $MMoO_4$-type compounds with different divalent cations, in which molybdenum may present tetrahedral coordination (scheelite-type structure, metal ionic radius M > 0.99 Å) or octahedral (wolframite-type structure, metal ionic radius M < 0.77 Å).

The experimental conditions adopted in the synthesis of copper molybdates can favour forming and obtaining different polymorphs that mainly exhibit specific properties and characteristics [33-37]. The alpha phase (α-$CuMoO_4$) has a triclinic structure and a particular group, where clusters [MoO_4] of tetrahedral symmetry are formed by coordinating the molybdenum atom to four oxygen atoms [38,39]. On the other hand, the gamma phase for copper molybdate (γ-$CuMoO_4$) exhibits a triclinic structure and has thermodynamic stability above 646 K [32,40].

In addition to the copper molybdate polymorphs reported above, there is also the occurrence of the minerals in the form of hydroxylated copper molybdates such as, lindgrenite - [$Cu_3(MoO_4)_2(OH)_2$], molybdofornacite - [$Pb_2Cu(MoO_4,CrO_4)(AsO_4, PO_4)OH$] and szenicsite - $Cu_3(MoO_4)(OH)_4$ [29]. Among these, lindgrenite is a semiconductor with a monoclinic structure and a particular group that exhibits octahedral symmetry clusters [CuO_6] and tetrahedral symmetry clusters [MoO_4] [30]. Concerning thermodynamic stability, the literature reports the structural conversion of lindgrenite to $Cu_3Mo_2O_9$, by the loss of a water molecule at temperatures close to 573 K [31].

Vilminot et al. [32] report the structural, optical and magnetic properties of lindgrenite nanocrystals synthesized by the hydrothermal method at 493 K for 24 h. On the other hand, Swain et al. [33], report the changes in the morphology of lindgrenite microspheres synthesized by the chemical precipitation method at room temperature for 15 min under constant pH (5.2). Recently, we have reported [30] the synthesis of microstructures composed of lindgrenite nanoplates obtained by sonochemical synthesis as well as their structural, optical, morphological, thermodynamic and antifungal properties.

Among the various synthesis methods, the sonochemical approach to obtain lindgrenite has numerous advantages. Overall, easy operation, fast processing, the obtainment of materials with a high degree of crystallinity and purity, size and morphology control, and the use of low-cost equipment, including ultrasonic washers [34-37].

Based on the information presented in the previous paragraphs, this work sought to study the structural, vibrational, optical and morphological properties of lindgrenite nanocrystals obtained by sonochemistry. Besides, we investigated the catalytic properties of the materials obtained in oleic acid esterification under different experimental conditions.

2. Materials and method

2.1. Synthesis of copper molybdate

In a typical sonochemical process, was dissolved 1 mmol of copper nitrate trihydrate – $Cu(NO_3)_2{\cdot}3H_2O$ (Sigma-Aldrich, purity 98–103%) and 1 mmol of sodium molybdate dihydrate – $Na_2MoO_4{\cdot}2H_2O$ (Sigma-Aldrich, purity > 99.9%) separately in falcon tubes (50 mL capacity) with 40 mL of distilled water, at room temperature, using Vortex equipment. We added the solution with molybdate ions in a beaker flask (120 mL capacity) and sonicated at room temperature using a Schuster washer machine equipment, L100 model, with power and frequency of 160 W and 40 kHz, respectively. Subsequently, was added the copper ion solution drop-by-drop, where a green suspension rapidly got formed, and then we sonicated this suspension for 1 h at room temperature. The green precipitate obtained was washed several times and centrifugated at 5.000 rpm for 5 min for each cycle, using distilled water to remove the Na^+ and NO_3^- ions. Finally, was dried the precipitate at 333 K for 48 h.

2.2. Characterization

The X-ray diffraction pattern of the sample was carried out by a Bruker diffractometer, D2Phaser model, using the copper anode as a source of radiation [λ(CuKα = 0.154184 nm] in the range 2θ from 5° to 100° with step size, current, and tension of 0.020°, 30 mA, and 40 kV, respectively.

We collected the Vibrational Raman spectrum of the sample using a Bruker confocal Raman spectrometer, SENTERRA model, in the range between 85 and 1100 cm^{-1}, exciting the sample using a red laser (λ = 785 nm) with output power, resolution, and integration time of 0.5 mW, 4 cm^{-1}, and 10 s^{-1}, respectively. We could observe the active vibrational modes in the infrared region (IR).

The lindgrenite nanocrystals' morphology was examinated by Field Emission Electron Microscopy (FE-SEM) operating an FEI Company microscope, Quanta FEG 250 model at different magnifications. Initially, 10 mg of sample was added into the Eppendorf (2 mL capacity) together with 1.5 mL of acetone and dispersed by ultrasonic radiation for 3 min. The suspension obtained was placed drop-by-drop onto the aluminium stub substrates and dried at 303 K for 30 min.

The nitrogen adsorption/desorption isotherms was performed using a Quantachrome device (Autosorb iQ Station 1) at 77.35 K, using 0.0195 g of sample, and initial treatment using final Outgas at 453 K for 6 h.

2.3. Catalytic performance of lindgrenite in the esterification of oleic acid

We evaluated the catalytic performance of the material obtained in this study through the oleic acid esterification for biodiesel synthesis (methyl oleate), where was added the oleic acid, methanol, and the catalyst (synthesized lindgrenite) in a stainless steel-coated Teflon reactor (25 mL capacity), without previous thermal activation of the catalyst using the following initial conditions: oleic acid:methanol molar ratio of 1:20, 373 K, and 5 wt% of catalyst concerning the acid mass, under magnetic stirring (690 rpm) for 3 h. Then, was separated the catalyst from reaction medium by centrifugation (5000 rpm for 5 min) and evaporated the excess methanol under reduced pressure. The percentage conversion of oleic acid to methyl oleate was calculated using

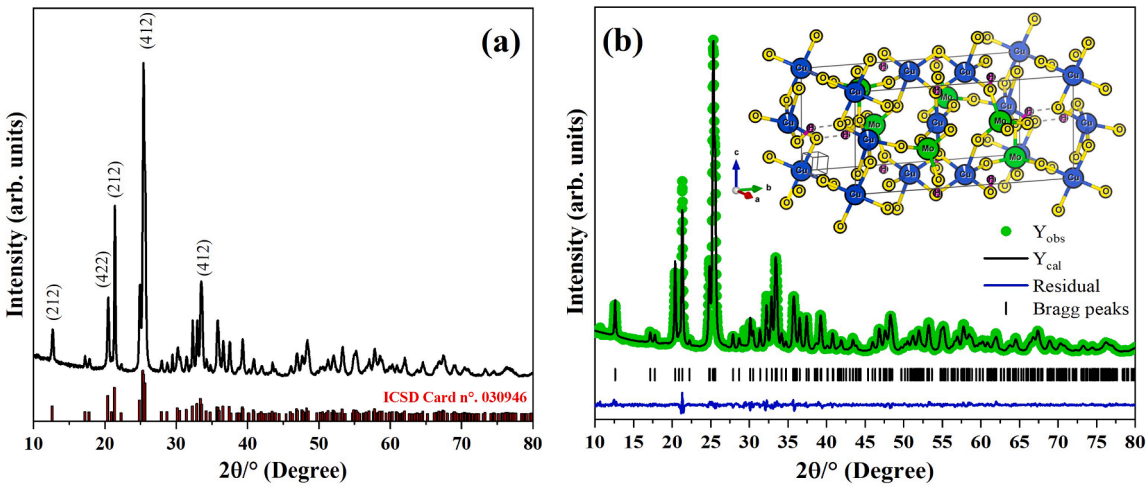

Fig. 1. (a) X-ray diffraction pattern and (b) Rietveld refinement plot of copper molybdate (lindgrenite) synthesized by the sonochemical method at room temperature for 1 h.

the final (A_f) and initial (A_i) acidity index (Eq. 1), titrating the reaction medium with a 0.1 mol L^{-1} NaOH solution [38,39].

$$\% \ Conversion = \frac{A_i - A_f}{A_i} \times 100 \quad (1)$$

The esterification process was also optimized, observing the effect of each parameter on the reaction, with the following parameters: reaction time (1, 3, 5, and 7 h), amount of catalyst (0, 2.5, 5.0, 7.5, and 10 wt%), acid:alcohol molar ratio (1: 3, 1: 5, 1:10, and 1:20) and temperature (353 K, 373 K, 393 K, and 413 K).

Also, was studied the stability of the catalyst through its recycling after successive reactions under optimized conditions. After each reaction, the catalyst was separated by centrifugation (5000 rpm for 5 min), washed it with hexane, and dried it at 353 K for 12 h.

3. Results and discussion

3.1. Structural characterization and Rietveld refinement of the XRD data

Fig. 1 shows the XRD pattern and Rietveld refinement plot for copper molybdate synthesized by the sonochemical method at room temperature for 1 h and standard Bragg peaks from card n° 30,946 of the Inorganic Crystal Structure Database – ICSD.

All diffraction peaks indexed for copper molybdate as-synthesized agree with the XRD pattern of lindgrenite (Fig. 1a) as observed at 2θ = 12.60°, 20.35°, 21.21°, 25.52°, and 33.5° were all characteristic of a monoclinic structure [40]. Therefore, these crystals present a monoclinic structure with a space group of *P*21*n*. Moreover, the sharp and intensity for all diffraction peaks suggest that there is a high crystallinity degree and also that they are ordered at long and short-range peaks [32]. We did not identify the secondary phase or reactants' diffraction peaks, confirming the high purity level and monoclinic structure as the only phase.

To better discuss the structural characteristics of the lindgrenite synthesized in this study, we performed structural refinement using the Rietveld method. The data from the lindgrenite experimental standard and the information contained in the ICSD card No. 030,946 were computed using the Fullprof free software version of April 2019. Therefore, we refined the lattice parameters (*a*, *b*, *c*, *α*, *β*, and *γ*) and atomic coordinates (*x*, *y*, and *z*, and profile shape parameters described by the Caglioti formula (*U*, *V*, and *W*), as well as the occupational (O_{cc}) and isotropic thermal (U_{iso}) factors. This study assigned the Pseudo-Voigt function to better adjust the diffraction peaks' intensity and profile and used a sixth-degree polynomial for background adjustment. We also monitored the quality of the computed data using the R-values for quality of fit (R_p, R_{wp}, R_e and χ^2).

Table 1
Structural Rietveld refinement results for lattice parameters (*a*, *b*, *c*, and *β*), the crystallite size (D_{hkl}) using the Scherrer's equation and unit cell volume (*V*) for lindgrenite from this work and reported by the literature.

Lattice parameters (Å)				V (Å^3)	D_{hkl} (nm)	Reference
a	*b*	*c*	β			
5.397 (4)	14.028 (3)	5.614 (6)	81.55 (6)	420.50 (9)	24.7(9)	this work
5.394 (1)	14.023 (3)	5.608 (1)	98.50 (1)	419.53 (14)		ICSD30946
5.386 (10)	14.001 (3)	5.601 (11)	98.53 (2)	417.73 (14)		[40]
5.3980 (2)	14.023 (4)	5.6183 (2)	98.497 (2)	420.22 (5)		[32]

Fig. 1(b) shows the graphical profile of the Rietveld refinement, including the experimental (Y_{obs}) and calculated (Y_{cal}) data, the residual ($Y_{obs} - Y_{cal}$) and Bragg peaks for the structure of lindgrenite. Thus, it is initially possible to infer that there is an excellent agreement between the experimental and computed data since there was a minimum residue (the difference between the experimental and theoretical intensities), corroborating the R-value ($\chi^2 = 1.93$). However, there was a slight tendency towards preferential orientation for the plane (2 1 2), similar to what was observed by Swain *et al.* [31] and Vilminot *et al.* [32]. This behaviour is probably associated with the anisotropic growth of this plane in the crystallization of nanostructures.

The Rietveld structural refinement results for the synthesized lindgrenite and the literature values are briefly shown in Table 1 and Table S1 (available at supplementary data).

Based on the results contained in Table S1, the atomic positions for the copper (Cu) and molybdenum (Mo) atoms did not present significant variations in the unit cell when compared with standard values [40]. On the other hand, the atomic positions for oxygen (O) and hydrogen (H) resulted in significant changes as a product of the distortion of Mo-O–H bonds in the tetrahedral [MoO_4] clusters, as well as the Cu–O–H bonds in the [CuO_5] clusters. These observed behaviours may be correlated to the process of the employed synthesis due to the high ultrasonic energy, which allows: (i) distortion of the Mo-O and Cu–O bonds; (ii) crystalline defects, and (iii) vacancies in oxygen atoms – $V_0^z = V_0^x$, $\dot{V}_0$ and $\ddot{V}_0$.

In agreement with the information obtained by the analysis of Table S1, the results obtained for the lattice parameters and unit cell

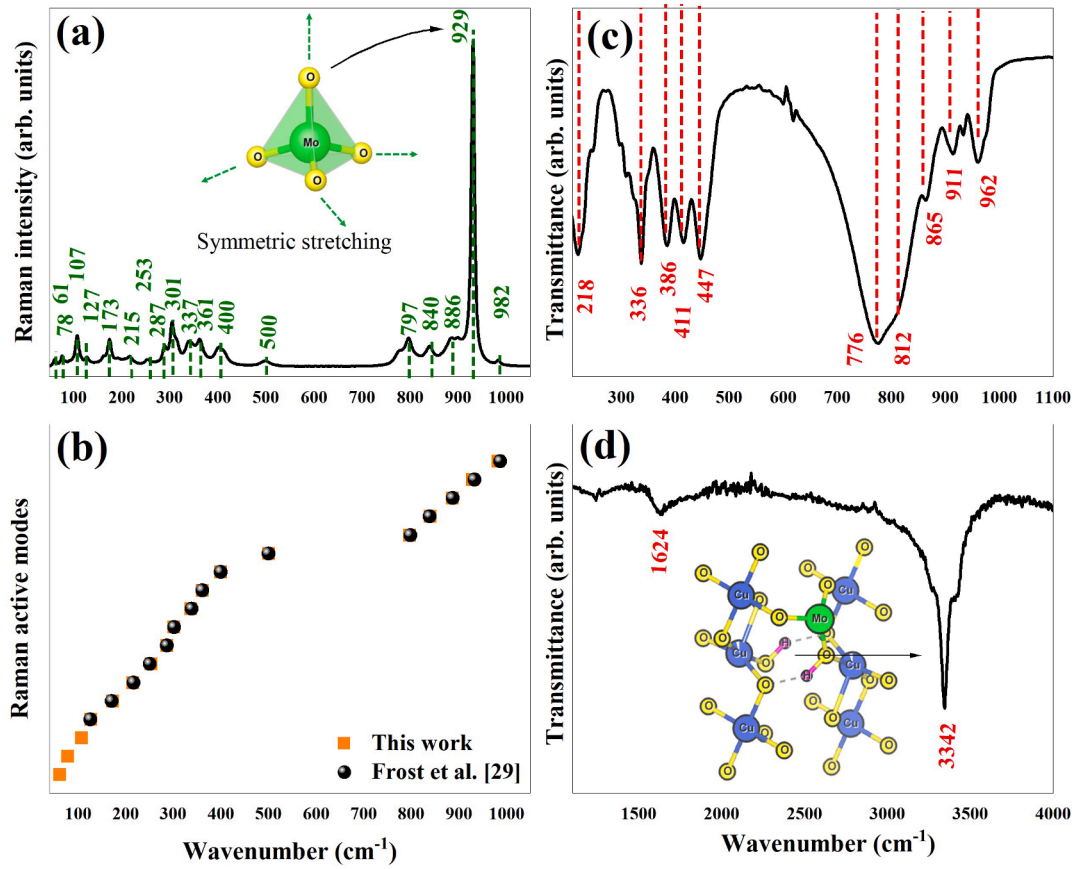

Fig. 2. (a) Raman spectrum, (b) relative peak position for all active modes of lindgrenite synthesized in this study and reported by Frost *et al.* [29], and (c) and (d) infrared spectrum of as-synthesized $Cu_3(MoO_4)_2(OH)_2$ in the region from 180 to 1100 cm^{-1} and 1200 to 4000 cm^{-1}, respectively.

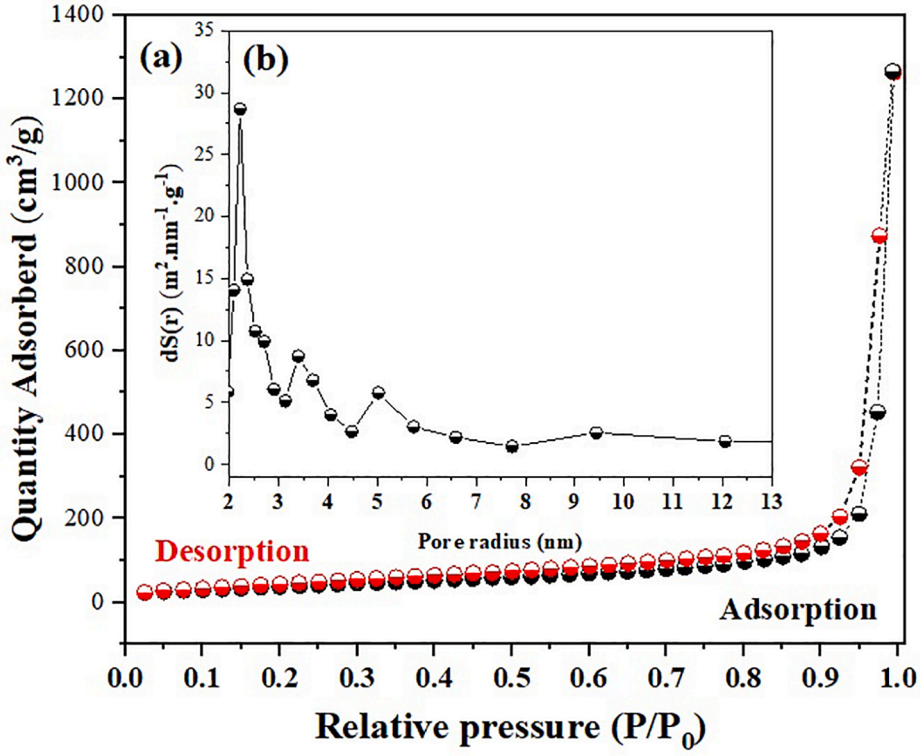

Fig. 3. (a) Nitrogen adsorption and desorption isotherm and (b) pore diameter by BJH method for as-synthesized lindgrenite.

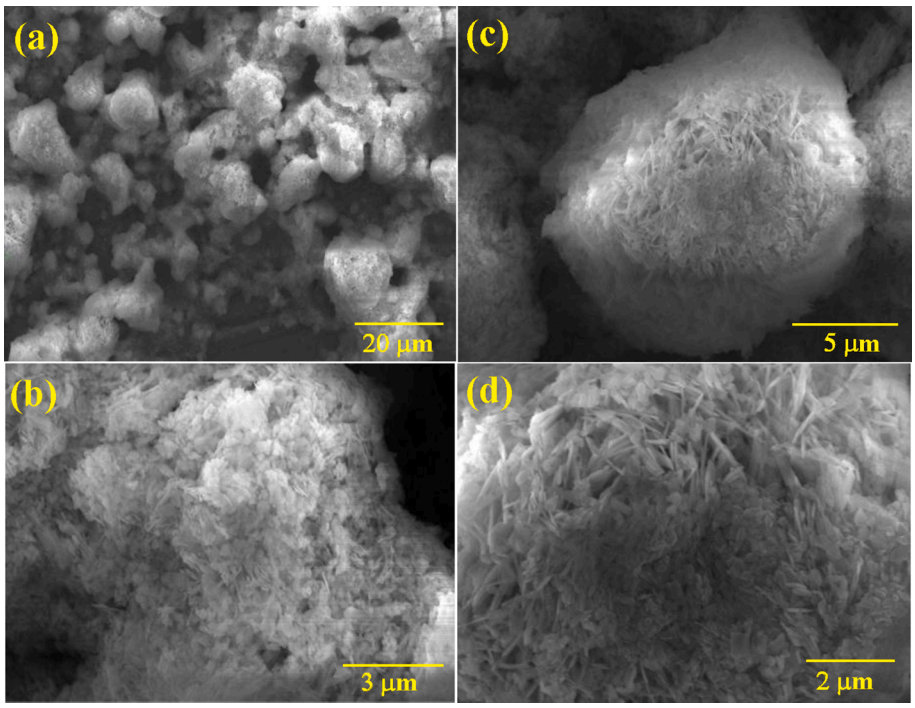

Fig. 4. Field Emission Electron Microscopy (FE-SEM) images of $Cu_3(MoO_4)_2(OH)_2$ at magnification of (a) 20, (b) 5, (c) 3 and (d) 2 μm.

volume confirm the expansion of the unit cell size compared to the literature values shown in Table 1. The angle β for the lindgrenite unit cell was smaller than that reported by the literature [32,41,42].

The crystallite size (D_{hkl}) of as-synthesized lindgrenite through the Scherrer's equation ($D_{hkl} = K\lambda/\mathrm{FWHM}\cos\theta$) [43], where K is the constant associated with the shape of nanoparticles ($k = 0.9$, spherical form), λ is the wavelength of the incident radiation (in this study CuKα = 0.15406 nm) while FWHM and θ are the full width at half maximum and the theta angle of diffraction peak for (4 1 2) plan at $2\theta = 25.52^{\circ}$. From this study, the D_{412} value obtained was 24.7(9) nm for lindgrenite nanoparticles. Rahimi-Nasrabadi *et al.* [28] reported a statistic study using the Taguchi robust method of optimization in the synthesis of copper molybdate in their experiments, obtaining particles sizes ranging from 80 to 252 nm.

3.2. Vibrational Raman and infrared spectroscopies

The Raman vibrational spectrum of lindgrenite was recorded to identify the active vibrational modes of lindgrenite and corroborate this information with the X-ray diffraction structural analysis.

Fig. 2a-d shows the Raman and infrared spectra of as-synthesized lindgrenite obtained by sonochemical route for 1 h at room temperature. From Fig. 2a, were well-identified eighteen active modes in the Raman spectrum of lindgrenite. Therefore, symmetric and anti-symmetric stretching active modes of M−O bonds from tetrahedral [MoO_4] clusters were identified in the range between 750 and 1000 cm^{-1} (Fig. 2a) in the Raman spectrum [44]. On the other hand, there are symmetric and anti-symmetric banding vibrations of O-Mo-O bonds in the interval from 300 to 500 cm^{-1}, characteristic of copper molybdates [29,44,45].

The bands ranging from 85 to 250 cm^{-1} are assigned to the rotational/translational active modes of tetrahedral MoO_4, which is also associated with the vibrational modes of Cu–O bonds in the octahedral [CuO_6] available in the crystal lattice [44]. All Raman active modes of as-synthesized lindgrenite are very similar to Raman's active mode positions reported by Frost et al. [29], as shown in Fig. 2b and Table S2 available in the supplementary data.

All active modes identified in infrared vibrational spectroscopy (Fig. 2c-d) align with the vibrational modes already reported in the literature [32,48]. We call attention to the bands referring to the asymmetric modes between 700 and 850 cm^{-1}, related to the Mo-O bonds contained in the [MoO_4] clusters [41], while in the range of 860 to 970 cm^{-1}, the identified bands indicate the vibrations of the free MoO_4^{2-} ions [32]. The medium intensity bands in 447 cm^{-1}, 1624 cm^{-1}, and 3342 cm^{-1} associated with the vibrations of the Cu-OH, O–H, and Cu–O–H connections, respectively, were also identified [31]. The lattice vibration bands and active modes associated with Cu–O vibrations were detected in 218 cm^{-1}, 336 cm^{-1}, 386 cm^{-1}, and 411 cm^{-1}.

3.3. N_2 adsorption/desorption isotherm

The specific surface area (*SA*) of lindgrenite nanocrystals was determined by the Brunauer–Emmett–Teller (BET) method from the N_2 adsorption/desorption data (Fig. 3).

The nitrogen adsorption/desorption isotherm profile was type III, characteristic of materials with poor interaction between the adsorbate and adsorbent [46], similar to what Swain *et al.* [31] reported. The *SA* estimated by the BET method was 70.77(1) $m^2\ g^{-1}$. In addition, the pore diameter calculated by the Barrett-Joyner-Halenda (BJH) method resulted in a higher amount of pores with diameters ranging between 2 and 6 nm.

3.4. Field emission scanning electron microscopy (FE-SEM)

We investigated the morphology of lindgrenite nanocrystals by FE-SEM as shown in parts of Fig. 4a-d using different magnifications, where it is possible to identify urchin-like clusters of nanoplates with micrometric dimensions and irregular shape and size. This morphological aspect suggests the self-assembly of nanoplates as an effect of the electrostatic attraction of surface charges, which, in the end, results in higher stability according to the morphology shown in Fig. 4a and 4d.

Swain *et al.* [33] reported micrometric flower-shaped structures composed of lindgrenite nanoplates using the aqueous chemical synthesis method at $pH \cong 7.1$ in 13 min. Xu *et al.* [41] reported different morphologies for lindgrenite using the hydrothermal method,

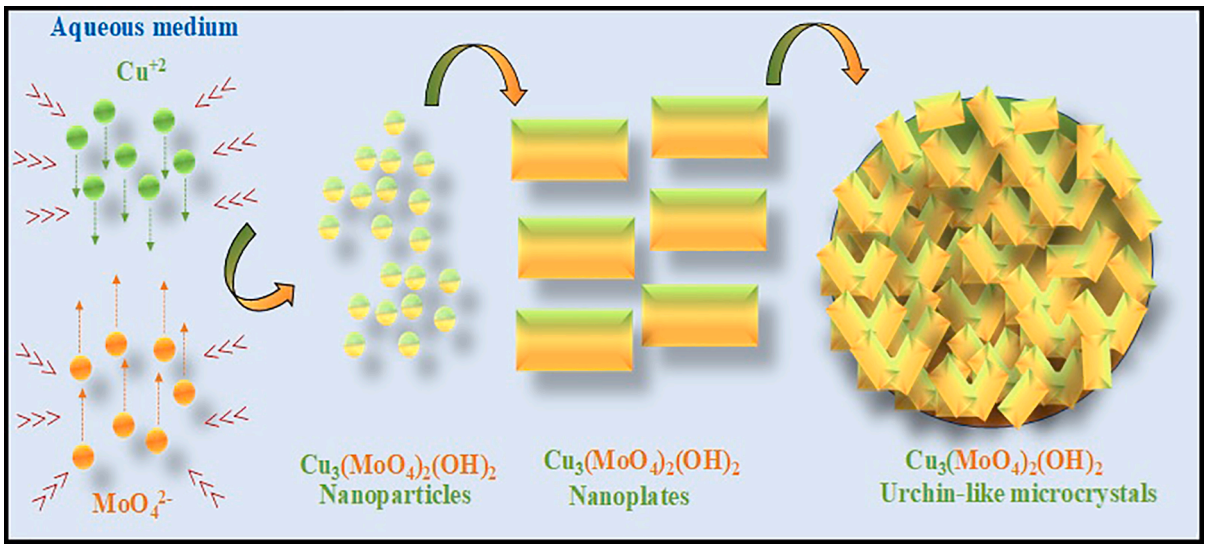

Fig. 5. Proposed scheme for the synthesis of lindgrenite urchin-like microcrystals using the sonochemical route at room temperature.

highlighting the dense and homogeneous microspheres composed of nanoplates, while Swain *et al.* [33] stated that the occurrence of $Cu_3(MoO_4)_2O$ microcrystals using thermal decomposition of flower-shaped lindgrenite mesostructures composed of nanocrystals. However, they have observed a distinctive aspect of the nanocrystals' shape and size in the nanoplates, similar to what we found in this study.

Based on these images and also on the study reported by Swain *et al.* [31], we suggest that during the process of formation of lindgrenite nanoplates, the solubilization of Cu^{2+} and MoO_4^{2-} ions from their precursors, copper nitrate trihydrate [$Cu(NO_3)_2 \cdot 3H_2O$] and sodium molybdate dihydrate ($Na_2MoO_4 \cdot 2H_2O$), in distilled water, occurs as described in the following Eq. (1) - (4).

$$3Cu(NO_3)_2 \cdot 3H_2O(s) \overset{H_2O}{\rightleftharpoons} 3Cu^{2+}(aq) + 6NO_3^-(aq) + 3H_2O(l) \quad (1)$$

$$2Cu^{2+}(aq) + HO^-(aq) \rightleftharpoons Cu_2(OH)^{3+}(aq) \quad (2)$$

$$Cu^{2+}(aq) + HO^-(aq) \rightleftharpoons Cu(OH)^{+}(aq) \quad (3)$$

$$Na_2MoO_4 \cdot 2H_2O(s) \overset{H_2O}{\rightleftharpoons} 2Na^+(aq) + MoO_4^{2-}(aq) + 2H_2O(l) \quad (4)$$

During the addition of the copper ion solution to the solution that contains the molybdate ions at room temperature and sonication ($\ggg$), the reactions that take place are expressed by Eq. (5) and (6).

$$MoO_4^{2-}(aq) + Cu_2(OH)_3^+(aq) \overset{\ggg}{\rightleftharpoons} [Cu_2(MoO_4)OH]^+(aq) \quad (5)$$

$$MoO_4^{2-}(aq) + Cu(OH)^+(aq) \overset{\ggg}{\rightleftharpoons} Cu(MO_4)OH]^-(aq) \quad (6)$$

Therefore, the lindgrenite nanoplates obtained combining the reactions of Eq. (5) and (6) may be represented in Eq. (7).

$$2MoO_4^{2-}(aq) + Cu_2(OH)_3^+(aq) + Cu(OH)^+(aq) \overset{\ggg,\ H_2O}{\rightleftharpoons} Cu_3(MoO_4)_2(OH)_2(s) \quad (7)$$

Finally, without the five water molecules in the products, we may represent the products seen in Eq. (8).

$$3Cu(NO_3)_2 \cdot 3H_2O(s) + 2Na_2MoO_4 \cdot 2H_2O(s) \overset{\ggg,\ H_2O}{\rightleftharpoons} Cu_3(MoO_4)_2(OH)_2(s) + 4NaNO_3(aq) + 2HNO_3(aq) + 3H_2O(l) \quad (8)$$

Fig. 5 shows the reaction mechanism schematically between ions in the aqueous medium under ultrasonic agitation in the formation of nanoplates and their reorganization to form the mesostructures, also described in Eqs. (1)–(8).

3.5. Catalytic assessment in the oleic acid esterification

After a careful search in the literature, we have found that this is the first study on the catalytic properties of copper molybdate regarding

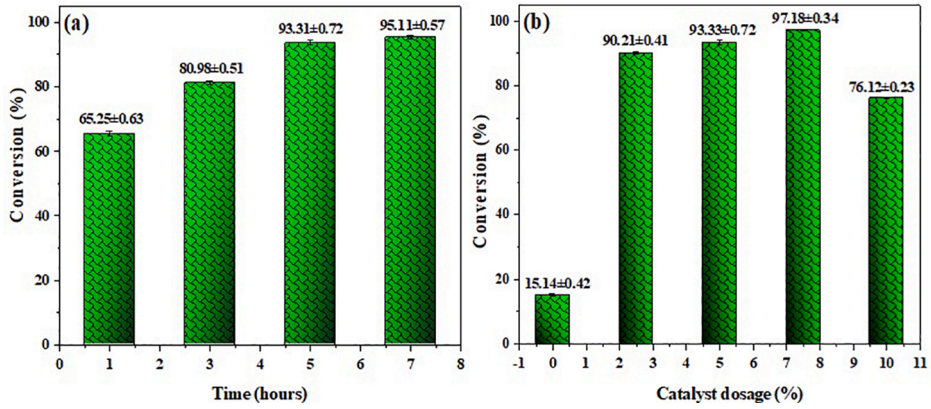

Fig. 6. (a) Effect of time on esterification of oleic acid with methanol under the following reaction conditions: 5 wt% of catalyst, acid:alcohol molar ratio of 1:20, at 373 K, (b) Effect of catalyst dosage under the following reaction conditions: acid:alcohol molar ratio of 1:20, 373 K, and 5 h of reaction.

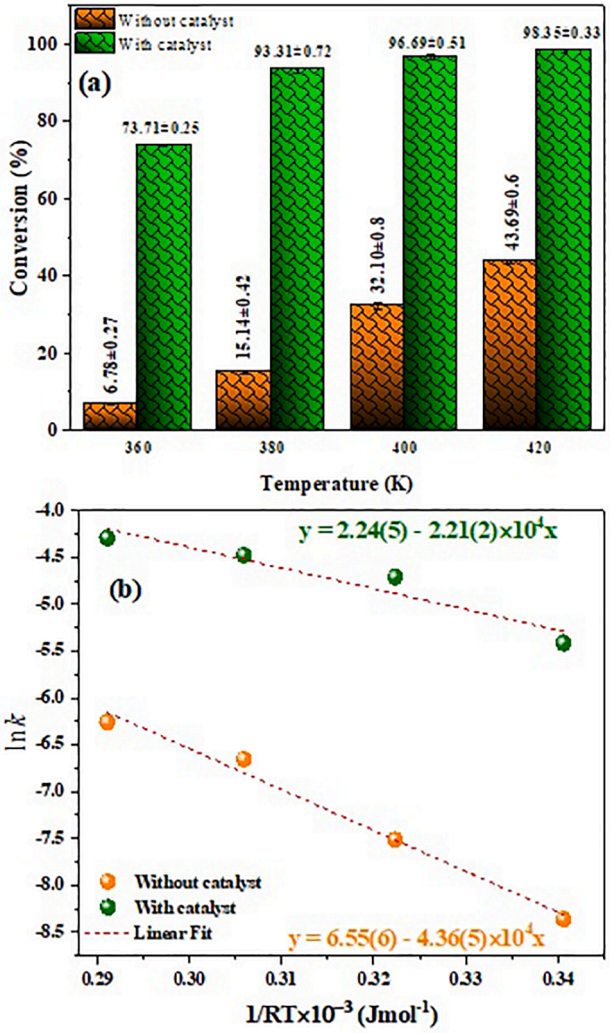

Fig. 7. (a) effect of temperature on the esterification of oleic acid. Reaction conditions: acid:methanol molar ratio of 1:20, 5 h reaction with 0 and 5 wt% catalyst. (b) Arrhenius plot ($\ln k_{app}$ vs. $1/RT$) for reactions with and without the catalyst.

lindgrenite – $Cu_3(MoO_4)_2(OH)_2$, applied in the synthesis of biodiesel by esterification of oleic acid. Therefore, the information reported in the consulted literature concerning the catalytic performance of compounds belonging to the class of molybdates ($MMoO_4$, where M is a metal), as well as molybdenum oxides (MoO_3), and copper oxide (CuO), among other heterogeneous catalysts applied in the oleic acid esterification reaction, were also used as comparative parameters.

3.5.1. Dependence of time and catalyst load

Fig. 6 shows the conversions of oleic acid into methyl oleate when the lindgrenite was used as a catalyst, with the influence of the reaction time (1, 3, 5, and 7 h) and catalyst dosage (0, 2.5, 5.0, 7.5, and 10%) assessed under the esterification reaction at a constant temperature of 373 K, oleic acid:methanol molar ratio of 1:20, and 5 wt% catalyst.

Because esterification reactions are strongly dependent on temperature and reaction time [47], the use of heterogeneous catalysts is decisive to reduce these parameters and, consequently, the final product's costs. Fig. 6.a shows the effect of reaction time on the conversion when applying 5 wt% of lindgrenite nanocrystals as a heterogeneous catalyst. Longer times resulted in greater conversions, reaching a plateau in 5 h of reaction (93.31(72) %). With 7 h of reaction, the conversion was 95.11(57) %, an increase of only 1.8% compared to the reaction processed in 5 h. Based on these results, we established 5 h as the optimal reaction time for subsequent esterification reactions.

Table 2
Comparison between catalysts, type of substrates (acid/oil), acid or oil:alcohol molar ratio, temperature (K), and conversions to methyl esters from this study and those reported in the literature.

Catalyst	Acid/oil	Acid/alcohol (mol/mol)	*T*(K)	Conversion (%)	Reference
$Cu_3(MoO_4)_2(OH)_2$	Oleic	1/20	353	73.71(25)*	This work
$Cu_3(MoO_4)_2(OH)_2$	Oleic	1/20	373	93.31(72)	This work
$Cu_3(MoO_4)_2(OH)_2$	Oleic	1/20	393	96.69(51)	This work
$Cu_3(MoO_4)_2(OH)_2$	Oleic	1/20	413	98.35(33)	This work
MF9S4	Oleic	1/60	403	84.2	[39]
MF9S4	Oleic	1/60	433	98.9	[39]
30% SiW_{12}/Hβ	Oleic	20/60	333	86	[51]
Na_2MoO_4	Soybean	1/48	393	72.6	[50]
CuO-Al_2O_3	Oleic	1/10	393	40.54	[52]

*The values expressed in parentheses refer to the sample standard deviations.

Fig. 6b shows the effect of the catalyst dosage on the oleic acid esterification, where we obtained a conversion of 15.14(42) % in the catalyst absence, resulting only from the effect of temperature on the reaction process. With only 2.5 wt% there was a significant increase in the conversion of oleic acid into biodiesel (90.21(41) %), proving the good catalytic activity of lindgrenite. By applying 5 wt% of catalyst, a plateau (93.33(72) %) was reached, with no significant increase in the catalyst's higher doses. On the other hand, when we added 10 wt% of catalyst to the reaction medium, there was a decrease of 21.06% in the conversion than the previous amount (7.5 wt%). Therefore, we suggest that in high doses of catalyst, there may occur: (i) low diffusion of the catalyst/alcohol/oleic acid [48]; (ii) inefficient reagent transfer rate due to increased viscosity [49]. Thus, to minimize the amount of catalyst while maintaining efficiency, an optimum dosage of 5 wt% of the catalyst was established.

Nakagaki *et al.* [50] reported using anhydrous sodium molybdate (Na_2MoO_4) as a heterogeneous catalyst in converting soybean oil into biodiesel. The authors emphasized the efficient participation of MoO_4^{2-} species, which exhibit acid character from Lewis sites with the polarisation of the O–H groups present in methanol and consequent favouring the reaction. Also, there was no significant increase in conversion when increasing catalyst dosage from 5 to 10 wt% under similar reaction conditions.

3.5.2. Dependence of temperature and activation energy (E_a)

Temperature is one of the main factors affecting the reactions, such as esterification, because it increases the system's entropy and, consequently, a more significant number of collisions between the substrate's molecules and the catalyst takes place. In Fig. 7a-b, it is possible to observe the effect of temperature on the conversion in the absence and presence of lindgrenite nanocrystals (catalyst), as well as the Arrhenius plot ($\ln k_{app}$ *versus* $1/RT$).

The reaction rate was proportional to the rise in temperature, providing an increase in conversion for the reactions catalyzed by lindgrenite and yielding a maximum conversion of 98.35(0.33) % at 413 K. The same trend occurred for non-catalyzed reactions, although with a maximum conversion of 43.69(25) % at the highest temperature used. Even at high temperatures, there was a big difference in conversion (approx. 55%), which shows this catalyst's importance in the reaction. This difference in conversion is even greater at lower temperatures. It is important to note that the conversion of the reactions catalyzed at 393 and 413 K did not significantly differ when considering the standard deviation. Therefore, we regarded the lower temperature (393 K as the optimum temperature for this process since lower temperatures result in cost reduction.

Based on these results, it was possible to observe the strong dependence on temperature of the oleic acid esterification in processed

Table 3
The activation energy of the esterification reactions of oleic acid in the presence of lindgrenite as a catalyst and comparison with other catalysts.

Catalyst	E_a (kJ mol^{-1})	Reference
Lindgrenite	22.1(2)*	This work
30%SiW_{12}/Hβ	49.8	[51]
H_2SO_4	42.0	[53]
TPA3/SBA-15	44.6	[54]
$SnCl_2$	46.69	[55]
PW(20)MFS	44.7	[38]
Mo/SiO_2	62.9	[56]
Amberlyst 15	74.4	[57]

*Values expressed in parentheses refer to the sample standard deviation.

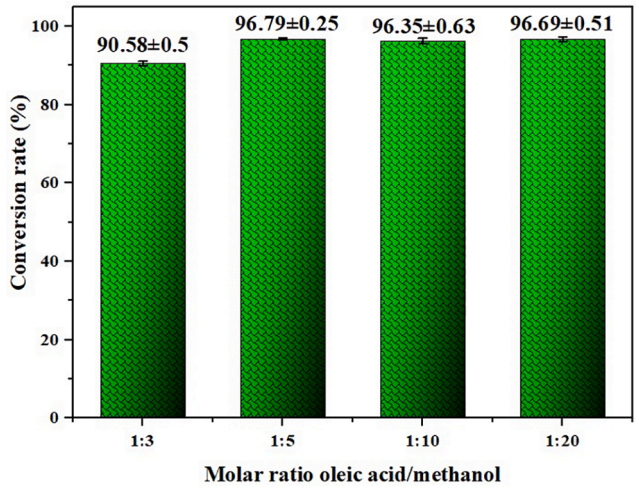

Fig. 8. Effect of acid:methanol molar ratio on the esterification of oleic acid at 393 K, 5 h of reaction, and 5 wt% of catalyst.

reactions. Also, the advantage of using lindgrenite as a catalyst was evident, providing a significant difference in each temperature studied when compared with the reactions processed in the absence of the catalyst. Some studies on the acid-catalyzed esterification reaction using temperatures equal or higher than the optimum temperature found in this work have shown lower conversions, even using higher acid:alcohol molar ratio and a higher catalyst dosage (Table 2).

We obtained the activation energies (E_a) of the catalyzed and non-catalyzed reactions through the Arrhenius equation (Eq. 9). However, the linearized equation (Eq. 10) was applied, where k_{app} is the apparent velocity constant for each reaction and its respective temperature (T) in Kelvin, R is the constant of the ideal gases, being 8.314 J mol^{-1} K^{-1}, and A_0 is the proportionality constant. Finally, the Ea values were obtained by the slope of the lines (Fig. 7b).

$$k_{app} = A_0 e^{-\frac{E_a}{RT}} \tag{9}$$

$$\ln k_{app} = \ln A_0 - \frac{E_a}{RT} + \ln k_0 \tag{10}$$

The graph shown in Fig. 7b clarifies the energetic difference between the catalyzed and non-catalyzed reactions, confirming how much lindgrenite reduces the activation energy and facilitates the occurrence of esterification. The Ea value of the non-catalyzed reaction was almost two times the Ea of the catalyzed reaction, being 43.6(5) and 22.1(2) kJ mol^{-1}, respectively. Further, when comparing the observed Ea of the reactions catalyzed by lindgrenite with the E_a found for esterification reactions with different catalysts, it was possible to observe that the first was significantly lower, making this catalyst promising for this application (Table 3).

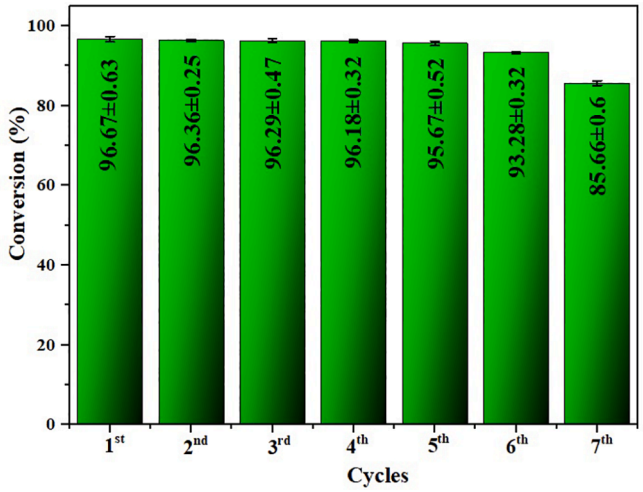

Fig. 9. Reutilization of solid catalyst (lindgrenite) on oleic acid esterification at optimized conditions: oleic acid:methanol molar ratio of 1:5, 393 K, 5 h of reaction 5 wt% of catalyst.

3.5.3. *Effect of the amount of methanol*

The amount of alcohol added in an esterification reaction is an important parameter to be investigated, considering that this type of reaction is potentially reversible [58]. Thus, we changed the molar ratio of oleic acid:methanol to observe its effect on the esterification reaction using lindgrenite as a catalyst (Fig. 8).

The results show an improvement in the conversion with the acid:methanol molar ratio, being 90.58(50)% in the 1:3 ratio and 96.79 (25)% in the 1:5 ratio. However, higher molar ratios did not significantly increase conversion compared to the acid:methanol molar ratio of 1:5.

The oleic acid:methanol molar ratio of 1:5 showed a high conversion (96.79%), considered the optimal ratio for this esterification process with the new catalyst, associated with the optimized experimental conditions. It is possible to observe that the results are considered expressive and economically viable compared to similar studies. Even in larger molar ratios, the conversions were much lower than those presented in this work (Table 2). Such conditions point to the use of lindgrenite as a very promising catalyst since reducing the amount of methanol in the reaction process reduces biofuel costs.

3.5.4. *Reusability of catalyst*

We evaluated the catalyst stability during seven consecutive esterification reactions under optimized conditions: 5 h of reaction, 5 wt% of catalyst, 393 K, and acid:alcohol molar ratio of 1:5. Fig. 9 shows the results related to the conversions obtained with the reuse of lindgrenite.

It is possible to observe no significant variations in the conversion over the first five cycles of catalyst reuse, obtaining values close to 96% with a slight reduction of 3% and 11% in the sixth and seventh cycles, respectively. It is worth noting that the only catalyst treatment between the cycles was washing with hexane and drying for subsequent application. A possible explanation for this reduction would be the addition of organic compounds on the material's surface, making it difficult for active sites to interact with the reagents [59]. Therefore, these results provide high stability to lindgrenite, a fundamental characteristic of high-efficiency catalysts.

In the study by Pinto et al. [60], the molybdenum trioxide (MoO_3) was obtained by hydrothermal synthesis and had its catalytic performance evaluated by transesterification reactions of soybean oil, when the catalyst also showed high stability. However, different experimental conditions were used: oil:alcohol molar ratio of 1:45, 423 K, 0.5 wt% of catalyst, and time 4 h.

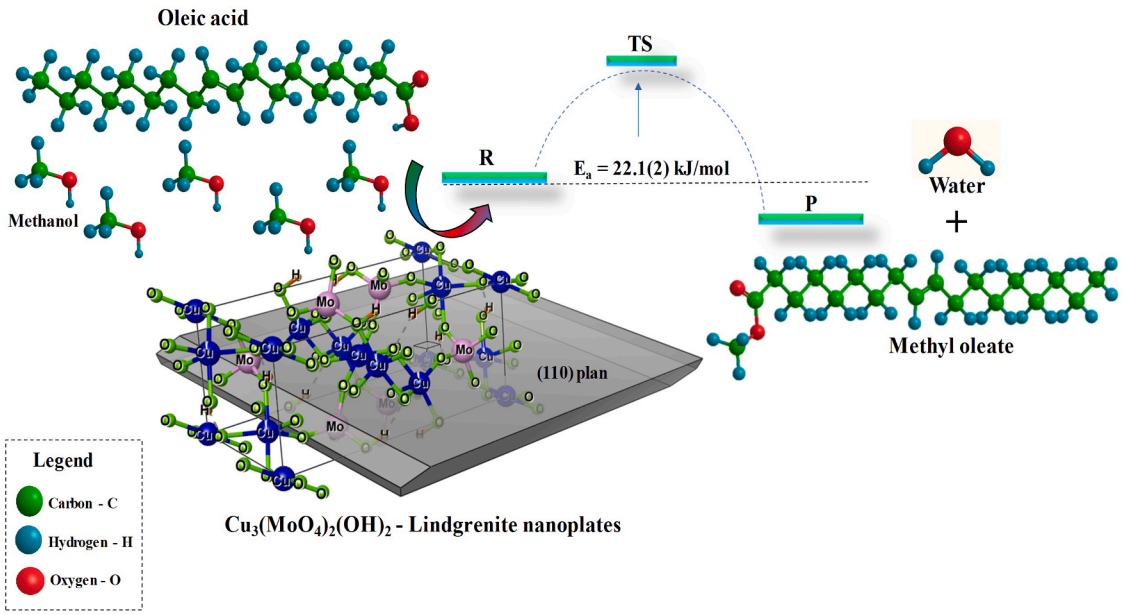

Fig. 10. Scheme for the catalytic reaction of oleic acid esterification on the lindgrenite surface using methanol.

3.5.5. Proposed mechanism of esterification using the lindgrenite as a heterogeneous catalyst

Based on the results of structural, vibrational, and morphological characterizations of lindgrenite observed in this study, we proposed a mechanistic model for the esterification of oleic acid (Fig. 10).

The high catalytic performance of lindgrenite observed in the esterification of oleic acid with methanol is likely due to two processes: The first, which we believe to be the main one, is based on the reactivity involving the Brønsted sites, occurring through the interaction of the molecules of the substrate (oleic acid) with Cu-OH bonds, arranged on the surface of nanoplates. This mechanism has been frequently reported for heterogeneous catalysts, among them zeolites [57], silica [56], kaolin [39], and 12-tungstophosphoric acid supported on kaolin [38]. The second proposed mechanism considers the reactivity of the substrate with the transition metal (M = Mo and Cu), which exhibits acid properties (Lewis acids), which were also presented in the reaction models reported for other catalysts, such as molybdenum trioxide – MoO_3 [60], ammonium molybdate – $(NH_4)_2MoO_4$ [61], sodium molybdate – Na_2MoO_4 [50], and magnesium molybdate – $MgMnO_4$ [62].

4. Conclusions

A novel catalyst, lindgrenite – $Cu_3(MoO_4)_2(OH)_2$, was synthesized through sonochemistry at room temperature. The structural characterization by X-ray diffraction and Rietveld refinement confirmed that the monoclinic structure (*P21n*) was the only phase present, showing the following lattice parameters: a = 5.397(4) nm, b = 14.028(3) nm, and c = 5.614(16) nm; unit cell volume V = 420.50(9) $Å^3$; and crystallite size D_{hkl} = 24.7(9) nm. All vibrational modes identified in Raman and infrared spectroscopies corroborate the structural results of lindgrenite. The images collected by scanning electron microscopy reveal the presence of urchin-like clusters composed of nanometric dimensions plates with a surface area of 70.77 (1) $m^2\ g^{-1}$. The catalytic performance of lindgrenite was evaluated through the esterification of oleic acid with methanol, resulting in conversions higher than 96% under optimized conditions: oleic acid:methanol molar ratio of 1:5, 393 K, 5 h of reaction, and 5 wt% of catalyst, besides the high stability of the catalyst even after 7 cycles of reuse. The high catalytic activity recorded results from the Bronsted and Lewis acidic sites, in which the first one would be more influential. Therefore, this work indicates the feasibility of producing an efficient and stable heterogeneous catalyst through a simple route for application in biodiesel synthesis.

CRediT authorship contribution statement

J.L. Silva Junior: Conceptualization, Formal analysis, Investigation, Methodology, Writing - original draft. **F.X. Nobre:** Conceptualization, Formal analysis, Writing - original draft. **F.A. de Freitas:** Data curation, Formal analysis, Investigation, Methodology. **T.A.F. de Carvalho:** Conceptualization. **S.S. de Barros:** Data curation. **M.C. Nascimento:** Data curation, Visualization. **L. Manzato:** Validation. **J.M.E. Matos:** Writing - review & editing. **W.R. Brito:** Project administration, Resources, Supervision. **Y. Leyet:** Project administration, Software. **P.R.C. Couceiro:** Project administration, Resources, Writing - review & editing.

Declaration of Competing Interest

The authors declare that they have no known competing financial interests that could have appeared to influence the work reported in this paper

Acknowledgements

The authors would like to thank Coordenação de Aperfeiçoamento de Pessoal de Nível Superior – CAPES and the Fundação de Amparo a Pesquisa do Estadodo Amazonas – FAPEAM for financial support. We also would like to thank the Laboratório de Síntese e Caraterização de Nanomateriais (LSCN) associado ao Sistema Nacional de Laboratórios em Nanotecnologias (SisNANO) - Processo CNPq 442601/2019-0 of Instituto Federal de Educação, Ciências e Tecnologia do Amazonas (IFAM-CMDI) and the Central Analítica of Instituto Federal de Educação, Ciências e Tecnologia do Amazonas (IFAM-CMC), for technical support.

Appendix A. Supplementary data

Supplementary data to this article can be found online at https://doi.org/10.1016/j.ultsonch.2021.105541.

References

[1] B.E.B. Costa, F.C. Rangel, R.S. da Cruz, Esterificação do ácido oleico utilizando aluminossilicato mesoporoso modificado com óxido de zircônio, Matéria (Rio Janeiro) 24 (2019), https://doi.org/10.1590/s1517-707620190001.0660.

[2] J. Brożyna, W. Strielkowski, A. Fomina, N. Nikitina, Renewable energy and EU 2020 target for energy efficiency in the Czech Republic and Slovakia, Energies 13 (2020) 965, https://doi.org/10.3390/en13040965.

[3] J. Bellosta von Colbe, J.-R. Ares, J. Barale, M. Baricco, C. Buckley, G. Capurso, N. Gallandat, D.M. Grant, M.N. Guzik, I. Jacob, E.H. Jensen, T. Jensen, J. Jepsen, T. Klassen, M.V. Lototskyy, K. Manickam, A. Montone, J. Puszkiel, S. Sartori, D. A. Sheppard, A. Stuart, G. Walker, C.J. Webb, H. Yang, V. Yartys, A. Züttel, M. Dornheim, Application of hydrides in hydrogen storage and compression: Achievements, outlook and perspectives, Int. J. Hydrogen Energy. 44 (15) (2019) 7780–7808, https://doi.org/10.1016/j.ijhydene.2019.01.104.

[4] R. Ganesan, S. Manigandan, M.S. Samuel, R. Shanmuganathan, K. Brindhadevi, N. T. Lan Chi, P.A. Duc, A. Pugazhendhi, A review on prospective production of biofuel from microalgae, Biotechnol. Rep. 27 (2020), e00509, https://doi.org/10.1016/j.btre.2020.e00509.

[5] P. Roy, N. Kumar Sinha, S. Tiwari, A. Khare, A review on perovskite solar cells: Evolution of architecture, fabrication techniques, commercialization issues and status, Sol. Energy. 198 (2020) 665–688, https://doi.org/10.1016/j.solener.2020.01.080.

[6] A. Datta, A. Hossain, S. Roy, An overview on biofuels and their advantages and disadvantages, Asian J. Chem. 31 (8) (2019) 1851–1858, https://doi.org/10.14233/ajchem10.14233/ajchem.2019.22098.

[7] I.M. Mendonça, F.L. Machado, C.C. Silva, S. Duvoisin Junior, M.L. Takeno, P.J. de Sousa Maia, L. Manzato, F.A. de Freitas, Application of calcined waste cupuaçu (Theobroma grandiflorum) seeds as a low-cost solid catalyst in soybean oil ethanolysis: statistical optimization, Energy Convers. Manag. 200 (2019) 112095, https://doi.org/10.1016/j.enconman.2019.112095.

[8] H.K. Jeswani, A. Chilvers, A. Azapagic, Environmental sustainability of biofuels: a review, Proc. R. Soc. A Math. Phys. Eng. Sci. 476 (2020) 20200351, https://doi.org/10.1098/rspa.2020.0351.

[9] S. de S. Barros, W.A.G. Pessoa Junior, I.S.C. Sá, M.L. Takeno, F.X. Nobre, W. Pinheiro, L. Manzato, S. Iglauer, F.A. de Freitas, Pineapple (Ananás comosus) leaves ash as a solid base catalyst for biodiesel synthesis, Bioresour. Technol. 312 (2020) 123569. 10.1016/j.biortech.2020.123569.

[10] C. Yue, P. Zhang, H. Wu, M. Fan, P. Jiang, Novel brønsted-lewis acid heterogeneous catalyst: functionalized imidazolium ferric salts@SBA-15 for efficient production of biodiesel, ChemistrySelect 4 (2019) 11275–11281, https://doi.org/10.1002/slct.201902753.

[11] E.O. Ajala, M.A. Ajala, I.K. Ayinla, A.D. Sonusi, S.E. Fanodun, Nano-synthesis of solid acid catalysts from waste-iron-filling for biodiesel production using high free fatty acid waste cooking oil, Sci. Rep. 10 (2020) 13256, https://doi.org/10.1038/s41598-020-70025-x.

[12] Chiara Pezzotta, Vijaykumar S. Marakatti, Eric M. Gaigneaux, Role of Lewis and Brønsted acid sites in resorcinol tert -butylation over heteropolyacid-based catalysts, Catal. Sci. Technol. 10 (23) (2020) 7984–7997, https://doi.org/10.1039/D0CY01030H.

[13] M. Tao, L. Xue, Z. Sun, S. Wang, X. Wang, J. Shi, Tailoring the synergistic bronsted-lewis acidic effects in heteropolyacid catalysts: applied in esterification and transesterification reactions, Sci. Rep. 5 (2015) 13764, https://doi.org/10.1038/srep13764.

[14] K.D. Kim, J. Kim, W.Y. Teoh, J.C. Kim, J. Huang, R. Ryoo, Cascade reaction engineering on zirconia-supported mesoporous MFI zeolites with tunable Lewis-Brønsted acid sites: a case of the one-pot conversion of furfural to γ-valerolactone, RSC Adv. 10 (2020) 35318–35328, https://doi.org/10.1039/d0ra06915a.

[15] K. Vasić, G. Hojnik Podrepšek, Ž. Knez, M. Leitgeb, Biodiesel production using solid acid catalysts based on metal oxides, Catalysts 10 (2020) 237, https://doi.org/10.3390/catal10020237.

[16] A. Bohlouli, L. Mahdavian, Catalysts used in biodiesel production: a review, Biofuels (2019) 1–14, https://doi.org/10.1080/17597269.2018.1558836.

[17] Bishwajit Changmai, Chhangte Vanlalveni, Avinash Prabhakar Ingle, Rahul Bhagat, Lalthazuala Rokhum, Widely used catalysts in biodiesel production: a review, RSC Adv. 10 (68) (2020) 41625–41679, https://doi.org/10.1039/D0RA07931F.

[18] R.M. Mohamed, G.A. Kadry, H.A. Abdel-Samad, M.E. Awad, High operative heterogeneous catalyst in biodiesel production from waste cooking oil, Egypt. J. Pet. 29 (1) (2020) 59–65, https://doi.org/10.1016/j.ejpe.2019.11.002.

[19] M.B. Navas, J.F. Ruggera, I.D. Lick, M.L. Casella, A sustainable process for biodiesel production using Zn/Mg oxidic species as active, selective and reusable heterogeneous catalysts, Bioresour. Bioprocess. 7 (2020) 4, https://doi.org/10.1186/s40643-019-0291-3.

[20] K.S. Moreira, L.S. Moura Júnior, R.R.C. Monteiro, A.L.B. de Oliveira, C.P. Valle, T. M. Freire, P.B.A. Fechine, M.C.M. de Souza, G. Fernandez-Lorente, J.M. Guisan, J. C.S. dos Santos, Optimization of the production of enzymatic biodiesel from residual babassu oil (Orbignya sp.) via RSM, Catalysts 10 (2020) 414, https://doi.org/10.3390/catal10040414.

[21] Anlian Zhu, Wanlu Feng, Zhiyong Li, Shuang Cheng, Qianhan Chen, Dongshuang Fan, Yuanyang Guo, Lingjun Li, Jianji Wang, Cleaner enzymatic production of biodiesel with easy separation procedures triggered by a biocompatible hydrophilic ionic liquid, Green Chem. 22 (6) (2020) 1944–1951, https://doi.org/10.1039/C9GC03796A.

[22] Hao Pang, Guoju Yang, Lin Li, Jihong Yu, Efficient transesterification over two-dimensional zeolites for sustainable biodiesel production, Green Energy Environ. 5 (4) (2020) 405–413, https://doi.org/10.1016/j.gee.2020.10.024.

[23] S. Niju, F.R. Raj, C. Anushya, M. Balajii, Optimization of acid catalyzed esterification and mixed metal oxide catalyzed transesterification for biodiesel production from Moringa oleifera oil, Green Process. Synth. 8 (2019) 756–775, https://doi.org/10.1515/gps-2019-0045.

[24] A. Navajas, I. Reyero, E. Jiménez-Barrera, F. Romero-Sarria, J. Llorca, L.M. Gandía, Catalytic performance of bulk and Al_2O_3-supported molybdenum oxide for the production of biodiesel from oil with high free fatty acids content, Catalysts 10 (2020) 158, https://doi.org/10.3390/catal10020158.

[25] N. Zamora-Romero, M.A. Camacho-Lopez, A.R. Vilchis-Nestor, V.H. Castrejon-Sanchez, G. Aguilar, S. Camacho-Lopez, M. Camacho-Lopez, Synthesis of molybdenum oxide nanoparticles by nanosecond laser ablation, Mater. Chem. Phys. 240 (2020), 122163, https://doi.org/10.1016/j.matchemphys.2019.122163.

[26] L. Dörner, C. Cancellieri, B. Rheingans, M. Walter, R. Kägi, P. Schmutz, M. V. Kovalenko, L.P.H. Jeurgens, Cost-effective sol-gel synthesis of porous CuO nanoparticle aggregates with tunable specific surface area, Sci. Rep. 9 (2019) 11758, https://doi.org/10.1038/s41598-019-48020-8.

[27] Reba Panigrahi, Santosh Kumar Sahu, Pradyota Kumar Behera, Subhalaxmi Panda, Laxmidhar Rout, $CuMoO_4$ bimetallic nanoparticles, an efficient catalyst for room temperature C−S cross-coupling of thiols and haloarenes, Chem. - A Eur. J. 26 (3) (2020) 620–624, https://doi.org/10.1002/chem.v26.310.1002/chem.201904801.

[28] M. Rahimi-Nasrabadi, S.M. Pourmortazavi, M. Khalilian-Shalamzari, Facile chemical synthesis and structure characterization of copper molybdate nanoparticles, J. Mol. Struct. 1083 (2015) 229–235, https://doi.org/10.1016/j.molstruc.2014.12.017.

[29] Ray L. Frost, Loc Duong, Matt Weier, Raman microscopy of the molybdate minerals koechlinite, iriginite and lindgrenite, Neues Jahrb. Fur Mineral. Abhandlungen. 180 (3) (2004) 245–260, https://doi.org/10.1127/0077-7757/2004/0180-0245.

[30] T.A. Feitosa de Carvalho, F.X. Nobre, A. de Lima Barros, A. Ghosh, A. de Almeida Lima e Silva, R. Oliveira dos Santos Fontenelle, M. Rita de Morais Chaves Santos, J. M. Elias de Matos, Investigation of optical, structural, and antifungal properties of lindgrenite obtained by conventional coprecipitation and ultrasound-assisted coprecipitation methods, J. Solid State Chem. 295 (2021) 121957. 10.1016/j.jssc.2021.121957.

[31] B. Swain, D.H. Lee, J.R. Park, C.G. Lee, K.J. Lee, D.W. Kim, K.S. Park, Synthesis of $Cu_3(MoO_4)_2(OH)_2$ nanostructures by simple aqueous precipitation: understanding the fundamental chemistry and growth mechanism, CrystEngComm 19 (2017) 154–165, https://doi.org/10.1039/c6ce02344d.

[32] Serge Vilminot, Gilles André, Mireille Richard-Plouet, Françoise Bourée-Vigneron, Mohamedally Kurmoo, Magnetic structure and magnetic properties of synthetic lindgrenite, $Cu^3(OH)^2(MoO^4)^2$, Inorg. Chem. 45 (26) (2006) 10938–10946, https://doi.org/10.1021/ic061182m10.1021/ic061182m.s001.

[33] B. Swain, D.-H. Lee, J.-S. Kim, C.-G. Lee, D.-W. Kim, K.-S. Park, Synthesis of flower-like $Cu_3[MoO_4]_2O$ from $Cu_3(MoO_4)_2(OH)_2$ and its application for lithium-ion batteries: structure-electrochemical property relationships, ChemElectroChem. 4 (2017) 2608–2617, https://doi.org/10.1002/celc.201700499.

[34] E.M. Cuerda-Correa, M.F. Alexandre-Franco, C. Fernández-González, Advanced oxidation processes for the removal of antibiotics from water. An overview, Water 12 (2019) 102, https://doi.org/10.3390/w12010102.

[35] N.G. Fagundes, F.X. Nobre, L.A.L. Basilio, A.D. Melo, B. Bandeira, J.C.C. Sales, J.C. S. Andrade, J. Anglada-Rivera, L. Aguilera, J. Pérez de la Cruz, Y. Leyet, Novel and simple way to synthesize $Na_2Ti_6O_{13}$ nanoparticles by sonochemical method, Solid State Sci. 88 (2019) 63–66, https://doi.org/10.1016/j.solidstatesciences.2018.11.014.

[36] S. Mallakpour, E. Azadi, Sonochemical protocol for the organo-synthesis of TiO2 and its hybrids: Properties and applications, Elsevier Inc., 2020. 10.1016/b978-0-12-819540-6.00011-5.

[37] F. Sedighi, A. Sobhani-Nasab, M. Esmaeili-Zare, M. Behpour, Fabricant and characterization of SrWO4 and novel silver-doped SrWO4 using co-precipitation method: their photocatalytic performances for methyl orange degradation, 9 (2019) 331–339. 10.22052/JNS.2019.02.015.

[38] Orivaldo da Silva Lacerda, Rodrigo Marinho Cavalcanti, Thaisa Moreira de Matos, Rômulo Simões Angélica, Geraldo Narciso da Rocha Filho, Ivoneide de Carvalho Lopes Barros, Esterification of oleic acid using 12-tungstophosphoric supported in flint kaolin of the Amazonia, Fuel 108 (2013) 604–611, https://doi.org/10.1016/j.fuel.2013.01.008.

[39] Luís Adriano S. do Nascimento, Laura M.Z. Tito, Rômulo S. Angélica, Carlos E.F. da Costa, José R. Zamian, Geraldo N. da Rocha Filho, Esterification of oleic acid over solid acid catalysts prepared from Amazon flint kaolin, Appl. Catal. B Environ. 101 (3-4) (2011) 495–503, https://doi.org/10.1016/j.apcatb.2010.10.021.

[40] R. Bao, Z. Kong, M. Gu, B. Yue, L. Weng, H. He, Hydrothermal synthesis and thermal stability of natural mineral lindgrenite1, Chem. Res. Chinese Univ. 22 (6) (2006) 679–683, https://doi.org/10.1016/S1005-9040(06)60189-X.

[41] Jiasheng Xu, Dongfeng Xue, Hydrothermal synthesis of lindgrenite with a hollow and prickly sphere-like architecture, J. Solid State Chem. 180 (1) (2007) 119–126, https://doi.org/10.1016/j.jssc.2006.09.030.

[42] S. Vilminot, M. Richard-plouet, M. Kurmoo, Magnetic Structure and Magnetic Properties of Synthetic Lindgrenite , 3 (n.d.).

[43] A.L. Patterson, The Scherrer Formula for X-Ray Particle Size Determination, Phys. Rev. 56 (1939) 978–982. 10.1103/PhysRev.56.978.

[44] H. Yang, R.A. Jenkins, R.M. Thompson, R.T. Downs, S.H. Evans, E.M. Bloch, Markascherite, Cu3(MoO4)(OH)4, a new mineral species polymorphic with szenicsite, from Copper Creek, Pinal County, Arizona, U.S.A., Am. Mineral. 97 (2012) 197–202. 10.2138/am.2012.3895.

[45] Ray L. Frost, Jocelyn Bouzaid, Ian S. Butler, Raman spectroscopic study of the molybdate mineral Szenicsite and comparison with other paragenetically related molybdate minerals, Spectrosc. Lett. 40 (4) (2007) 603–614, https://doi.org/10.1080/00387010701301220.
[46] K.S.W. Sing, Reporting physisorption data for gas/solid systems with special reference to the determination of surface area and porosity (Recommendations 1984), Pure Appl. Chem. 57 (1985) 603–619. 10.1351/pac198557040603.
[47] R. Shokrani, M. Haghighi, Textural evolution of hierarchical nanostructured ZSM-5 via sono-hydrothermal design by various carbon shapes for efficient biodiesel production, Appl. Catal. B Environ. 271 (2020), 118940, https://doi.org/10.1016/j.apcatb.2020.118940.
[48] W.C. De Abreu, C.V.R. De Moura, J.C.S. Costa, E.M. De Moura, Strontium and nickel heterogeneous catalysts for biodiesel production from macaw oil, J. Braz. Chem. Soc. 28 (2017) 319–327, https://doi.org/10.5935/0103-5053.20160181.
[49] J. Nisar, R. Razaq, M. Farooq, M. Iqbal, R.A. Khan, M. Sayed, A. Shah, I. Ur Rahman, Enhanced biodiesel production from Jatropha oil using calcined waste animal bones as catalyst, Renew. Energy. 101 (2017) 111–119, https://doi.org/10.1016/j.renene.2016.08.048.
[50] Shirley Nakagaki, Alesandro Bail, Vannia Cristina dos Santos, Victor Hugo Rodrigues de Souza, Heron Vrubel, Fábio Souza Nunes, Luiz Pereira Ramos, Use of anhydrous sodium molybdate as an efficient heterogeneous catalyst for soybean oil methanolysis, Appl. Catal. A Gen. 351 (2) (2008) 267–274, https://doi.org/10.1016/j.apcata.2008.09.026.
[51] Nilesh Narkhede, Anjali Patel, Biodiesel production by esterification of oleic acid and transesterification of soybean oil using a new solid acid catalyst comprising 12-tungstosilicic acid and zeolite hβ, Ind. Eng. Chem. Res. 52 (38) (2013) 13637–13644, https://doi.org/10.1021/ie402230v.
[52] Mojgan Hashemzehi, Naser Saghatoleslami, Hamed Nayebzadeh, Microwave-assisted solution combustion synthesis of spinel-type mixed oxides for esterification reaction, Chem. Eng. Commun. 204 (4) (2017) 415–423, https://doi.org/10.1080/00986445.2016.1273831.
[53] D.A.G. Aranda, R.T.P. Santos, N.C.O. Tapanes, A.L.D. Ramos, O.A.C. Antunes, Acid-Catalyzed Homogeneous Esterification Reaction for Biodiesel Production from Palm Fatty Acids, Catal. Letters. 122 (2008) 20–25. 10.1007/s10562-007-9318-z.
[54] V. Brahmkhatri, A. Patel, 12-Tungstophosphoric acid anchored to SBA-15: An efficient, environmentally benign reusable catalysts for biodiesel production by esterification of free fatty acids, Appl. Catal. A Gen. 403 (2011) 161–172, https://doi.org/10.1016/j.apcata.2011.06.027.
[55] A. Cardoso, S. Neves, M. Da Silva, Esterification of oleic acid for biodiesel production catalyzed by $SnCl_2$: a kinetic investigation, Energies 1 (2008) 79–92, https://doi.org/10.3390/en1020079.
[56] A. Bail, V.C. dos Santos, M.R. de Freitas, L.P. Ramos, W.H. Schreiner, G.P. Ricci, K. J. Ciuffi, S. Nakagaki, Investigation of a molybdenum-containing silica catalyst synthesized by the sol-gel process in heterogeneous catalytic esterification reactions using methanol and ethanol, Appl. Catal. B Environ. 130–131 (2013) 314–324, https://doi.org/10.1016/j.apcatb.2012.11.009.
[57] Jitendra K. Satyarthi, Darbha Srinivas, Paul Ratnasamy, Influence of surface hydrophobicity on the esterification of fatty acids over solid catalysts, Energy Fuels 24 (3) (2010) 2154–2161, https://doi.org/10.1021/ef1001452.
[58] M. Olkiewicz, N.V. Plechkova, M.J. Earle, A. Fabregat, F. Stüber, A. Fortuny, J. Font, C. Bengoa, Biodiesel production from sewage sludge lipids catalysed by Brønsted acidic ionic liquids, Appl. Catal. B Environ. 181 (2016) 738–746, https://doi.org/10.1016/j.apcatb.2015.08.039.
[59] E. Betiku, A.M. Akintunde, T.V. Ojumu, Banana peels as a biobase catalyst for fatty acid methyl esters production using Napoleon's plume (Bauhinia monandra) seed oil: a process parameters optimization study, Energy 103 (2016) 797–806, https://doi.org/10.1016/j.energy.2016.02.138.
[60] B.F. Pinto, M.A.S. Garcia, J.C.S. Costa, C.V.R. de Moura, W.C. de Abreu, E.M. de Moura, Effect of calcination temperature on the application of molybdenum trioxide acid catalyst: screening of substrates for biodiesel production, Fuel 239 (2019) 290–296, https://doi.org/10.1016/j.fuel.2018.11.025.
[61] S. Sadighi, S.K. Masoudian Targhi, Preparation of Biofuel from palm oil catalyzed by ammonium molybdate in homogeneous phase, Bull. Chem. React. Eng. Catal. 12 (2017) 49, https://doi.org/10.9767/bcrec.12.1.486.49-54.
[62] M. Karthikeyan, S. Renganathan, G. Baskar, Production of biodiesel from waste cooking oil using $MgMoO_4$-supported TiO_2 as a heterogeneous catalyst, Energy Sources Part A Recover. Util. Environ. Eff. 39 (2017) 2053–2059, https://doi.org/10.1080/15567036.2017.1371815.